



## Real Time 3D Observations of Portland Cement Carbonation at CO<sub>2</sub> Storage Conditions

Elvia A. Chavez Panduro, Benoit Cordonnier, Kamila Gawel, Ingrid Borge, Jaisree Iyer, Susan A. Carroll, Leander Michels, Melania Rogowska, Jessica Ann Mcbeck, Henning Osholm Sorensen, et al.

### ► To cite this version:

Elvia A. Chavez Panduro, Benoit Cordonnier, Kamila Gawel, Ingrid Borge, Jaisree Iyer, et al.. Real Time 3D Observations of Portland Cement Carbonation at CO<sub>2</sub> Storage Conditions. Environmental Science and Technology, 2020, 54 (13), pp.8323-8332. 10.1021/acs.est.0c00578 . hal-03723611

**HAL Id: hal-03723611**

**<https://hal.science/hal-03723611>**

Submitted on 15 Jul 2022

**HAL** is a multi-disciplinary open access archive for the deposit and dissemination of scientific research documents, whether they are published or not. The documents may come from teaching and research institutions in France or abroad, or from public or private research centers.

L'archive ouverte pluridisciplinaire **HAL**, est destinée au dépôt et à la diffusion de documents scientifiques de niveau recherche, publiés ou non, émanant des établissements d'enseignement et de recherche français ou étrangers, des laboratoires publics ou privés.

# Real Time 3D Observations of Portland Cement Carbonation at CO<sub>2</sub> Storage Conditions

Elvia A. Chavez Panduro,\* Benoît Cordonnier, Kamila Gawel, Ingrid Børve, Jaisree Iyer, Susan A. Carroll, Leander Michels, Melania Rogowska, Jessica Ann McBeck, Henning Osholm Sørensen, Stuart D. C. Walsh, François Renard, Alain Gibaud, Malin Torsæter, and Dag W. Breiby\*



Cite This: *Environ. Sci. Technol.* 2020, 54, 8323–8332



Read Online

ACCESS |



Metrics & More

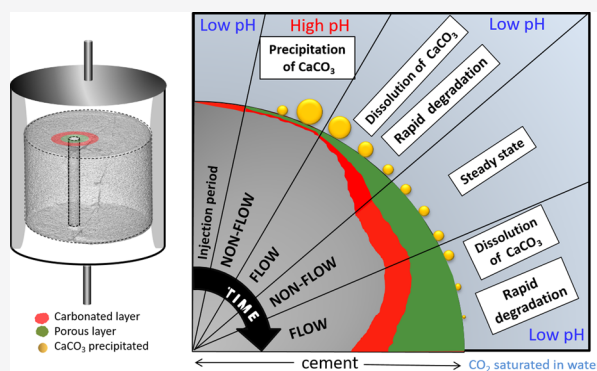


Article Recommendations



Supporting Information

**ABSTRACT:** Depleted oil reservoirs are considered a viable solution to the global challenge of CO<sub>2</sub> storage. A key concern is whether the wells can be suitably sealed with cement to hinder the escape of CO<sub>2</sub>. Under reservoir conditions, CO<sub>2</sub> is in its supercritical state, and the high pressures and temperatures involved make real-time microscopic observations of cement degradation experimentally challenging. Here, we present an in situ 3D dynamic X-ray micro computed tomography ( $\mu$ -CT) study of well cement carbonation at realistic reservoir stress, pore-pressure, and temperature conditions. The high-resolution time-lapse 3D images allow monitoring the progress of reaction fronts in Portland cement, including density changes, sample deformation, and mineral precipitation and dissolution. By switching between flow and nonflow conditions of CO<sub>2</sub>-saturated water through cement, we were able to delineate regimes dominated by calcium carbonate precipitation and dissolution. For the first time, we demonstrate experimentally the impact of the flow history on CO<sub>2</sub> leakage risk for cement plugging. In-situ  $\mu$ -CT experiments combined with geochemical modeling provide unique insight into the interactions between CO<sub>2</sub> and cement, potentially helping in assessing the risks of CO<sub>2</sub> storage in geological reservoirs.



## INTRODUCTION

Finding a solution to the global CO<sub>2</sub> emissions problem has become increasingly important in recent years.<sup>1</sup> One of the most promising mitigating measures is its sequestration in depleted oil and gas reservoirs,<sup>2</sup> using cement to seal the wellbores. However, the risk of CO<sub>2</sub> leakage to the atmosphere has hindered large scale implementation. According to the Intergovernmental Panel on Climate Change (IPCC), leakage along wellbores imposes the largest risk of CO<sub>2</sub> migration toward the surface.<sup>2</sup> These leakage pathways can exist both in the cement plug or in the annular region between the casing and the caprock and can be formed during drilling, completion, or abandonment.<sup>3</sup> One potential problem is that the sealing properties of the cement will be affected when the CO<sub>2</sub> reacts with cement along the pre-existing leakage paths. To assess the risk related to CO<sub>2</sub> sequestration in depleted oil and gas reservoirs, an enhanced understanding of the influence of CO<sub>2</sub> on Portland cement under reservoir conditions is critical.

When CO<sub>2</sub> saturated water is in contact with cement at reservoir conditions, a series of thoroughly investigated chemical reactions lead to cement carbonation.<sup>4,5</sup> Three distinct reaction zones form in cement upon carbonation and propagate away from the cement/carbonated-water interface with time.<sup>4,6</sup> The first stage of carbonation involves dissolution

of portlandite (Ca(OH)<sub>2</sub>, CH in cement chemistry notation) to form a portlandite depleted zone. In the second stage, a carbonated zone forms by the precipitation of dissolved portlandite as calcium carbonate (CaCO<sub>3</sub>, CC) upon reaction with carbonic acid. The last stage of carbonation is the dissolution of this newly formed CC through a bicarbonation process producing an amorphous porous silica zone.<sup>4,7–12</sup> The carbonation rate in cement depends on the chemical (portlandite content, calcium silicate hydrate content) and physical properties of cement (porosity, tortuosity) as well as the processing conditions (curing time, temperature, pressure, and fluid flow rate).<sup>13–16</sup>

It has been observed that fractures present in cement can either close (self-seal) or open upon carbonation. Self-sealing is usually caused by precipitation of CC<sup>17,18</sup> but may also be a result of cement swelling<sup>10</sup> or cement deformation,<sup>19</sup> whereas fracture opening is typically caused by the dissolution of

Received: January 29, 2020

Revised: June 6, 2020

Accepted: June 11, 2020

Published: June 11, 2020



ACS Publications

© 2020 American Chemical Society

8323

<https://dx.doi.org/10.1021/acs.est.0c00578>  
*Environ. Sci. Technol.* 2020, 54, 8323–8332

cement compounds<sup>20</sup> and/or stresses induced by crystal precipitation.<sup>21</sup> Several studies attempting to explain the sealing behavior of fractures have emphasized the importance of flow rate, either in terms of Darcy flux<sup>22</sup> or residence time.<sup>12,19,23</sup> In connected fractures running parallel to the wellbore, the CO<sub>2</sub> fluid can reach high flow rates driven by pressure gradients.<sup>24,25</sup> Newell et al. stated that the potential leakage rates calculated from a natural CO<sub>2</sub> producer with a wellbore permeability between 1 and 10 mD (inferred over a single 3 m interval) are around 0.3–3 mL/h.<sup>24</sup> Laboratory experiments on samples subjected to flow of CO<sub>2</sub>-fluids are typically in the range of 1–100 mL/h.<sup>6,10,12,26</sup> Wolterbeek et al. stated that the flow rate can vary considerably with time and even display pulsed or periodic flow behavior.<sup>27</sup> Field studies report that the occurrence of periodic flow include Taylor-bubble formation, competition between capillary and buoyancy effects, and pressure driven aperture.<sup>28–31</sup> Thus, more work is needed to quantitatively understand the impact of flow history on the sealing behavior of fractures, as in real CO<sub>2</sub> storage sites, the reservoir pressures driving leakage are expected to change over time.

Owing to its complexity, only few field studies have characterized CO<sub>2</sub> well integrity. Carey et al. studied Portland cement retrieved from an enhanced oil recovery (EOR) reservoir at the SACROC unit in Texas.<sup>32</sup> Crow et al. studied cement from a natural CO<sub>2</sub> reservoir in the Dakota sandstone formation.<sup>33</sup> In both studies, even if the cement was altered due to CO<sub>2</sub> exposure, it was concluded that the cement could still provide an effective barrier to CO<sub>2</sub> migration. Ex-situ static and flow-through laboratory experiments that aim to understand the carbonation processes in cement have several limitations. An understanding of the dynamics of the carbonation processes in such experiments is difficult to obtain because it is challenging to decouple the effects of carbonation from the effects of depressurization prior to observing the sample.<sup>26</sup> We have recently reported kinetics of carbonation of Portland cement based on an in situ X-ray computed tomography experiment; however, due to (flux) limitations of the in-house X-ray tomography setup, the sample cell had to be kept relatively thin and transparent, thus preventing the use of realistic stress and fluid pressure conditions.<sup>34</sup>

Here, in an effort to directly observe the cement carbonation at relevant reservoir conditions, i.e., representative axial and radial confining stresses as well as high pore pressure and temperature, we report in situ microtomography ( $\mu$ -CT) experiments using a unique X-ray tomography-compatible triaxial deformation apparatus (HADES).<sup>35</sup> We observed, in 3D and real-time, cement reaction fronts propagating through the cement sample as well as precipitation and dissolution of CaCO<sub>3</sub> in leakage paths present in the cement exposed to varying CO<sub>2</sub> saturated-water flow conditions. The experiment thus provided unique data that can be used for refining geomechanical and geochemical numerical models on the cement carbonation and self-sealing processes.

## MATERIALS AND METHODS

**Sample Preparation.** Class G cement (High Sulfate Resistant Well Cement, Norcem AS) was mixed according to an API recommended practice<sup>36</sup> with a water/cement mass ratio of 0.44. The slurry was poured into a cylindrical plastic mold with a diameter of 5 mm and a length of 4 mm. A smooth cylindrical channel running through the sample was artificially made by having a nylon fishing line (diameter 0.4

mm) in the cement slurry during curing. The total curing time was about 2 weeks. Additionally, for comparisons of reaction behavior, a rougher “natural” fracture, also extending through the sample length, was purposely introduced by gently cleaving the specimen with a scalpel immediately prior to the experiment. The resulting two pieces were snugly fit back together inside the confining rubber gasket. See SI S1 for details.

**Experimental Setup.** The cement sample was measured using the HADES triaxial deformation apparatus.<sup>35</sup> The sample equipment comprises the cell itself, two pumps that control the confining and axial pressure, and two injection pumps that control the fluid pressure (Figure S1); see Renard et al.<sup>35</sup> The cement sample was placed inside a rubber gasket, together with two sandstone spacers (7% porosity, 5 mm diameter, 3 mm length) above and below to achieve a homogeneous flow of CO<sub>2</sub>. The CO<sub>2</sub>-saturated water was pressurized to 28 MPa. The CO<sub>2</sub>-saturated water was injected axially into the cement sample from the top. The working fluid pressure and temperature were 28 MPa and 80 °C. The cement sample was kept under realistic axial and radial confining pressures of 31 and 30 MPa, respectively. During the experiment, different CO<sub>2</sub> flow regimes ranging from hydrostatic (stagnant) to purging were imposed to test the dependence of flow history on the reaction kinetics, cf. Figure 1b and SI S1.

**Synchrotron Measurement.** X-ray tomography data were acquired at the ESRF ID19 beamline, using a high photon energy of 84 keV to enable the X-ray radiation to be transmitted through the titanium walls of the deformation apparatus. The sample–detector distance was 1200 mm, giving edge-enhanced phase contrast.<sup>37</sup> 2D projections were obtained with a PCO Dimax detector with a pixel size of 6.45  $\mu$ m and an exposure time of 0.05 s. For each time step, a full  $\mu$ -CT data set consisting of 2000 radiographs (projections) over 180° were acquired. In total, 103 time-steps (full tomograms) were recorded over a period of nearly 20 h. The data were reconstructed using PyHST2<sup>38</sup> involving filtered back-projection coupled with the phase contrast algorithm.<sup>37</sup> Three-dimensional image analysis was done using ImageJ; see more details in SI S3.

**Geochemical Model.** Chemical reaction calculations in an idealized 2D geometry were performed to relate the experimental observations to solution chemistry. In the absence of experimental data on ion concentrations, pH, and saturation indices of the minerals, the model predictions provide information that allows us to corroborate our hypotheses explaining the experimental observations. The experimentally calibrated model (calibrated to a different set of experimental observations)<sup>19,39</sup> couples flow of carbonated water through fractures at cement–cement/cement-caprock interfaces, advective and diffusive transport of the dissolved chemical species along the fracture, diffusive transport of the chemical species within the cement, and geochemical reactions between the cement and carbonated water. The model can predict calcite precipitation in a fracture but is limited to predicting uniform precipitation instead of precipitation at specific nucleation sites. In addition, the model assumes that once calcite precipitates at a fracture surface, it passivates the surface and prevents the growth of the porous amorphous silicate layer until the surface precipitate is completely dissolved. A detailed description of the model can be found in SI S5 and other references.<sup>16,19,39</sup>



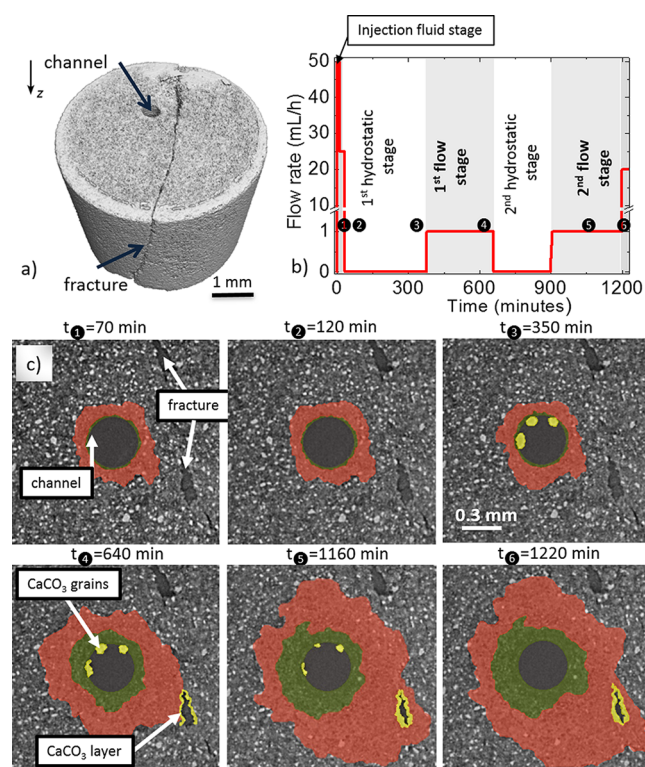


**Figure 1.** Overview of the in situ  $\mu$ -CT experiment of carbonation of Portland cement in the presence of  $\text{CO}_2$ . (a) Perspective 3D view of the Portland cement sample, with the channel and the fracture indicated by arrows. (b) The flow history of  $\text{CO}_2$  saturated water through the sample during the experiment. (c) Lateral  $\mu$ -CT cross-sections at  $z = 2$  mm showing the region near the channel, obtained at the indicated times. The images show the evolution of the carbonated zone (red) and porous silica zone (green) in the cement, and precipitation/dissolution of calcium carbonate (yellow) in the channel and the fracture. The raw images without the color segmentation are provided in Figure S11.

**Geomechanical Calculation.** Digital volume correlation (DVC) analysis was performed to extract the evolution of the displacement field within the sample, using the software Tomowarp2;<sup>40</sup> see also refs 41 and 42. DVC analysis cross-correlates voxel intensities in series of tomograms in order to derive the displacement field as a function of time. For these experiments, we used a 10-voxel node spacing, averaging the displacement field over subvolumes of  $10^3$  voxels, in a central region of the sample centered around the channel. From DVC analysis of the whole sample, it can be seen (cf. SI) that the whole sample tilted slightly. Consequently, after removing sporadic unphysically large outlier values from the displacement field, the averaged lateral displacements (locally corresponding to trivial sample translation) were subtracted before the lateral displacement field was plotted superposed on slices from the tomography data.

## RESULTS AND DISCUSSION

**Overview of Experimental Observations.** The cylindrical Portland cement sample was produced with both a smooth “artificial” cylindrical inner channel (diameter  $\sim 0.4$  mm) and a rough “natural” fracture around  $\sim 0.5$  mm away from the channel, both extending through the full length of the sample (Figure 1a). The specimen was designed to maximize the amount of information that could be retrieved during the

limited duration of synchrotron access. The cement was exposed to the pressure (28 MPa) and temperature (80 °C) conditions corresponding to a  $\sim 2$  km depth in a depleted oil reservoir.<sup>43</sup> Alternating flow and hydrostatic (nonflow) conditions of  $\text{CO}_2$  saturated water were imposed on the sample to delineate precipitation versus dissolution-dominated regimes (SI Note 1 and Figure 1b). Water was chosen instead of the 0.5 M NaCl brine commonly used in order to increase the  $\text{CO}_2$  saturation and hence the reaction rates. The cement specimen was monitored with synchrotron X-ray  $\mu$ -CT, enabling the 3D morphological impact of the chemical reactions (Figure 1c) to be followed in time. We observed the progression of the reaction zones in the cement, the competing precipitation vs dissolution dynamics of CC observed in both the channel and the fracture upon exposure to  $\text{CO}_2$ , and the concomitant mechanical specimen deformation. When the sample was subjected to the confining and axial pressures at the beginning of the experiment, most of the cavities in the natural fracture were closed, thus reducing the fracture aperture. CC precipitation was observed at the ends of the fracture (cf. Figures 2 and 4). Therefore, the CC deposits

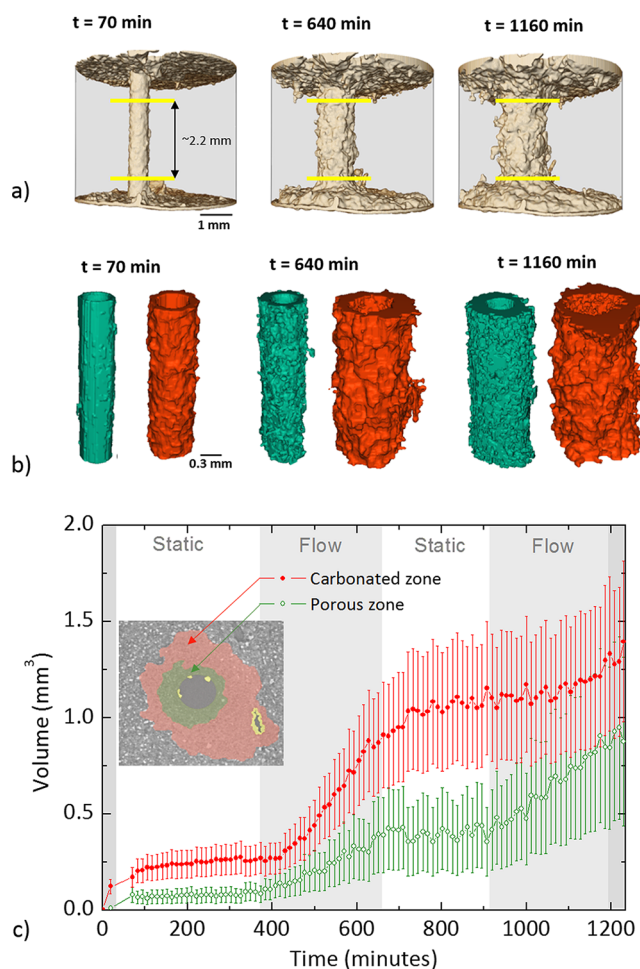


**Figure 2.** Reaction fronts in the cement as a function of time retrieved from  $\mu$ -CT analysis. (a) 3D volume rendering of the whole specimen, showing reacted cement in yellow, at 70, 640, and 1160 min, (b) 3D rendering of carbonated (red) and porous silica zones (green), and (c) volume evolution of the reacted zones within the middle part of the sample, as delineated with yellow lines in part a. The inset shows a segmented cross-section sample.

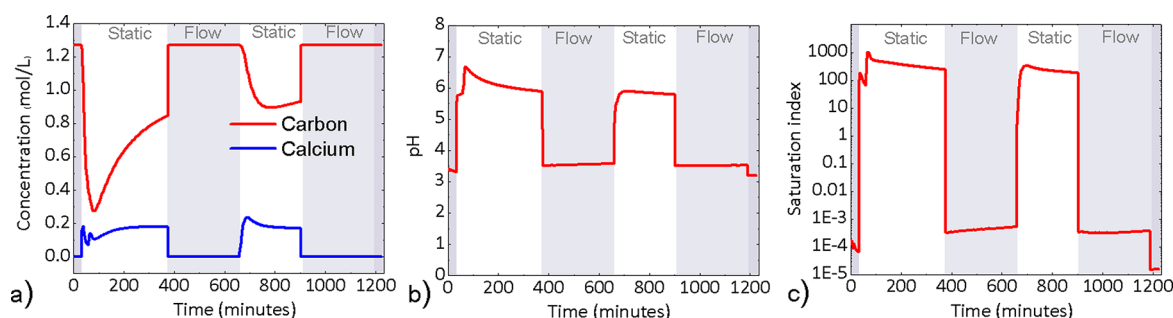


**Figure 3.** Numerical geochemical model predictions. (a) Calcium and carbon concentrations, (b) pH, and (c) saturation index of calcite at the outlet face of the sample as a function of time.

and the confining stress applied to the sample prevented fluid transport in the fracture, so essentially all the flowing fluid was forced to go through the channel. Interestingly, both in the channel and the fracture, precipitation of  $\text{CC}$  was observed, but their respective precipitation processes were different.

**Cement Carbonation and Reaction Zones Propagation.** During the experiment, changes in the density of cement were observed at all the surfaces that were in contact with  $\text{CO}_2$ -saturated water, i.e., at both ends of the cement cylinder and around the channel; see Figure 2. The mass density of the carbonated zone increased compared to the unreacted cement due to the abundance of  $\text{CC}$ .<sup>11</sup> Calcium carbonate has higher density compared to the calcium hydroxide present in the unreacted cement, thus increasing the attenuation, which is observed in the  $\mu$ -CT images as brighter gray scale levels. When the carbonated zone progresses into the cement sample, the amorphous porous silica zone develops in between the carbonated layer and the cement surface (Figure 1), giving a decrease in the X-ray attenuation; see also SI S2. The carbonated zone and the porous silica zone were clearly discernible in the reconstructed cross-section images, including how they propagated over time (Figure 1c, S11). The portlandite depleted zone predicted by several previous studies could arguably be observed in the  $\mu$ -CT images as a slightly less dense region with a thickness of  $\sim 20\ \mu\text{m}$  outside the carbonated zone (SI S4). As shown by the model predictions in SI S5, the thickness of the different layers depends on the composition of the unreacted cement, with higher portlandite content in the cement resulting in thinner reacted layers.<sup>16</sup>

The temporal evolution of the volumes of the carbonated and porous silica zones (Figure 2 and S14) shows that the growth rates of the carbonated and porous silica regions were significant under flow conditions while they were small and negligible under hydrostatic conditions. The volumetric growth rates of the carbonated and porous silica regions were found to be  $2.5 \times 10^{-3} \pm 8 \times 10^{-5}$  and  $1 \times 10^{-3} \pm 5 \times 10^{-5}\ \text{mm}^3/\text{min}$  for the first flow phase and  $7.0 \times 10^{-4} \pm 1.1 \times 10^{-4}$  and  $1.8 \times 10^{-3} \pm 8 \times 10^{-5}\ \text{mm}^3/\text{min}$  for the second flow phase, consistent with previous reports of cement alteration slowing with time.<sup>14,19</sup> This slowdown arises from a change in the properties of the cement during the course of experiment, in particular, the growth of the dense carbonated zone<sup>14,44</sup> with low permeability that hinders the transport of reactants into the unreacted cement. In addition, the distance of diffusion of the reactants from the channel to the unreacted cement increases with time, which also contributes to slowing down the carbonation processes. We note also that while in the first flow phase, the growth rate of the carbonated layer was higher than the rate of the porous silica layer, in the second flow

phase, the porous silica layer grew faster than the carbonated layer.

The results confirm that the rate of cement alteration depends on the  $\text{CO}_2$  flow conditions, with rapid cement degradation under flow conditions<sup>5,44,45</sup> and slow degradation for hydrostatic conditions.<sup>4,6</sup> The flow rate controls the  $\text{CO}_2$ -saturated water composition (calcium and carbonate content, pH) in the channel and determines the rate of cement degradation because diffusive transport of reactants into the cement is proportional to their concentration gradients. During the hydrostatic stages, the concentration gradient of the reactants is smaller due to the reactant consumption and the accumulation of products in the channel fluid.

The geochemical modeling results are given in Figure 3, giving predictions of the temporal evolution of the total calcium (i.e., aqueous  $\text{Ca}^{2+}$ ,  $\text{CaHCO}_3^+$ ,  $\text{CaCO}_3$ ) and total carbon concentrations (i.e., aqueous  $\text{CaHCO}_3^+$ ,  $\text{CaCO}_3$ ,  $\text{CO}_2$ ,  $\text{H}_2\text{CO}_3$ ,  $\text{HCO}_3^-$ ,  $\text{CO}_3^{2-}$ ) at the outlet face of the sample. In the convective stages, the effluent carbon content is expected to be almost equal to the inlet carbon concentrations. The modeling supports that the carbon content at the outlet in the second hydrostatic stage is higher than that in the first one, implying that less carbon is consumed in the reaction with the cement during the second hydrostatic phase.

The porous silica zone grew during the flow stages and did not propagate during the hydrostatic stages. The conditions that promote  $\text{CC}$  dissolution and propagation of the porous silica zone are low pH and undersaturation of the surrounding solution with respect to  $\text{CC}$ .<sup>46</sup> During flow conditions, the pH in the channel is expectedly low (cf. Figure 3) due to the constant supply of carbonic acid and the washing away of the calcium ions, which keeps the water undersaturated and promotes dissolution of  $\text{CC}$ . In the hydrostatic stages, the model results support the intuition that the pH increases and saturation with respect to calcite is rapidly reached in the channel (within less than 3 min), which prevents further dissolution of the  $\text{CC}$  in the cement and thus effectively arrests the growth of the porous silica zone. The growth of the porous silica zone is probably reaction rate-limited rather than transport-limited because the porous permeable layer is not expected to hinder diffusion of the reactants in the same way that the carbonated layer does.<sup>44</sup> Nevertheless, we observe differences in the propagation rate of the porous silica zone in both flow stages. The volumetric growth of the porous silica layer during the second flow stage was faster than that in the first flow stage, perhaps because of the progressively increasing surface area from which it is dissolved as the porous silica zone grows.

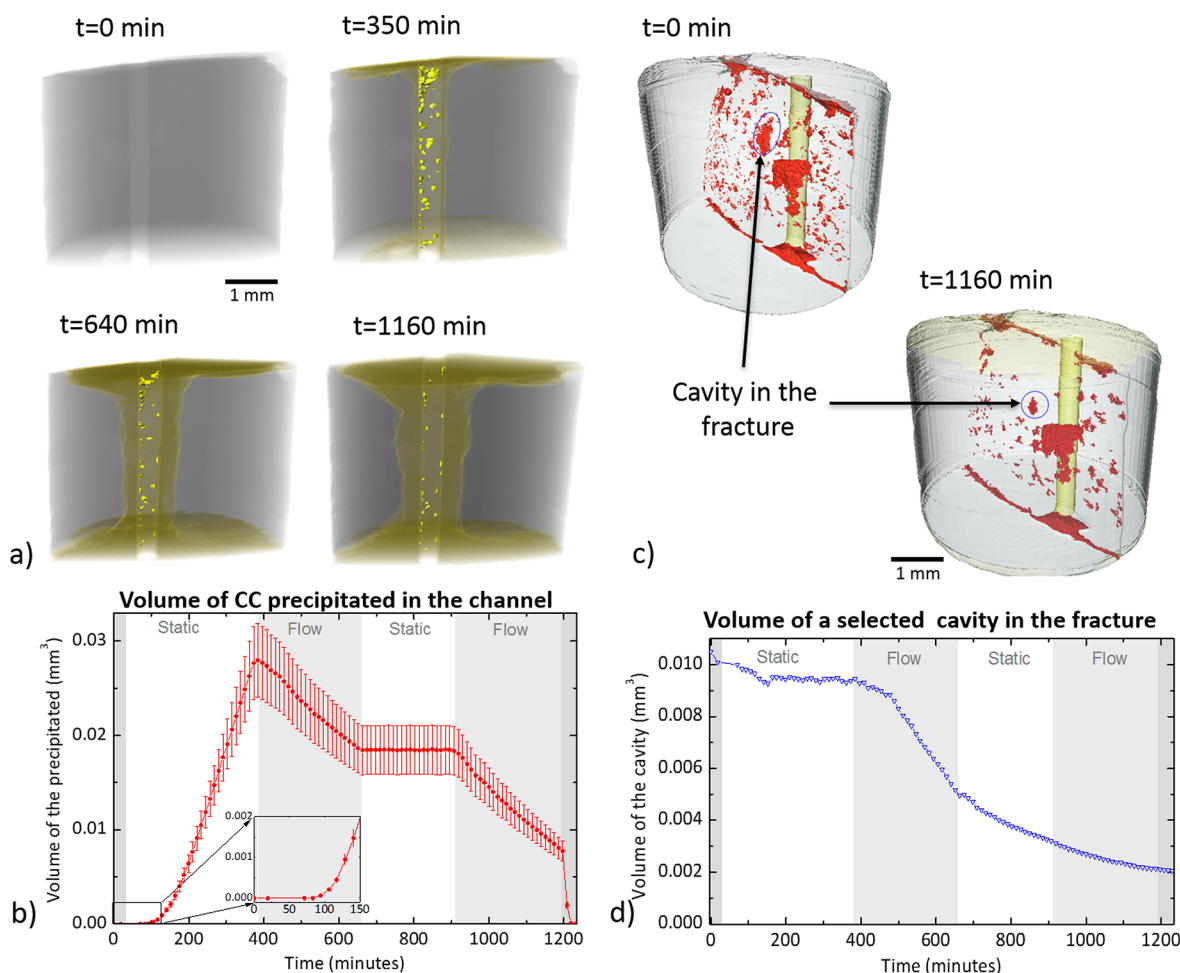


**Figure 4.** Precipitation in the channel and the fracture. (a) 3D visualization of precipitated CaCO<sub>3</sub> in the channel, the crystals are highlighted in sharp yellow, reacted cement in yellow-brown and the unreacted cement cylinder is in semitransparent gray. (b) Time evolution of the precipitated CaCO<sub>3</sub> volume in the channel. The inset shows a zoomed-in view of the first 150 min (c) 3D visualization of the fracture (in red) before and after CO<sub>2</sub> exposure. The channel is represented in transparent yellow. (d) Time evolution of the volume of the selected cavity in the fracture shown in part c.

**Precipitation of CaCO<sub>3</sub> in the Channel.** During the first hydrostatic phase, CC crystals precipitated onto the walls of the smooth cylindrical channel. Figure 4 shows the temporal evolution of the precipitated CaCO<sub>3</sub> volume. During the first 90 min, no precipitation in the channel was observed. The total volume of CC precipitated in the channel grew almost linearly between  $t = 150$  and  $370$  min with a growth rate of  $1.2 \times 10^{-4} \pm 10^{-6}$  mm<sup>3</sup>/min. The precipitation was first observed at the top of the channel, close to the CO<sub>2</sub>-saturated water inlet, which suggests a concentration gradient along the channel, cf. Figure S15. Similarly, it is likely that the CO<sub>2</sub>-fluid exposure to the end surface of the cement specimen (cf. Figure 2a) may have slightly preconditioned the fluid (reduced the concentration of carbonic acid) before entering the channel. As soon as the flow was introduced, the precipitates in the channel started to dissolve at a rate of  $3.6 \times 10^{-5} \pm 5 \times 10^{-7}$  mm<sup>3</sup>/min. When the flow was paused after  $t = 650$  min, the dissolution also stopped, and no crystal growth was observed during the second hydrostatic stage. At  $t = 900$  min, the flow was re-established, resulting in resumed dissolution of CC. Further increase in the flow rate from 1 to 20 mL/h toward the end of the experiment resulted in a ten times higher dissolution rate, completely emptying the cylindrical channel of solid CaCO<sub>3</sub>.

At the temperature and pressure conditions used in the experiment, calcium carbonate should have precipitated in the channel in the form of aragonite.<sup>47</sup> However, the shape of the growing crystals was nearly spherical, suggesting that the polymorph formed could be vaterite.<sup>48,49</sup> The model prediction of a pH between 6 and 7 in the channel (Figure 3b) during the static phase further supports the hypothesis that the polymorphic form of the precipitated CC could be vaterite.<sup>50</sup> Due to the complexity of the CC precipitation process, other techniques will be needed to conclude about the exact nature of this polymorph.

Precipitation of CC requires oversaturation of the water with CC. The saturation index of calcite plotted in Figure 3 is defined as  $[a_{Ca^{2+}}][a_{CO_3^{2-}}]/K_{sp}$  where  $a_i$  denotes the activity of the  $i^{\text{th}}$  species, and  $K_{sp}$  is the solubility product constant. The saturation index depends on pH, being lower at alkaline and higher at basic conditions.<sup>51</sup> The precipitation of CC inside the channel started after an induction time of  $t \sim 90$  min into the first hydrostatic phase. This was the time needed for the water in the channel to reach oversaturation and for the particles to grow to a detectable size. A similar delay in precipitation was predicted by the geochemical numerical model (SI S5). While CC did not precipitate in the channel during the induction time, a slight growth of the carbonation zone was observed.



When oversaturation was reached in the channel, the carbonated zone stopped growing and  $\text{CC}$  precipitated in the channel until the end of the first hydrostatic stage. The precipitation started near the inlet where oversaturation was first reached. The precipitation stopped and dissolution of  $\text{CC}$  in the channel started right after the flow of  $\text{CO}_2$ -saturated water was introduced (Figure 4b). At the high flow rate used in our experiment (1 mL/h, cf. Figure 1), the calculated saturation index of calcite in the carbonated water is well below 1 (Figure 3c). In such a significantly undersaturated solution,  $\text{CC}$  dissolved continuously.

During the second hydrostatic stage, which lasted for 250 min,  $\text{CC}$  did not precipitate in the channel, in stark contrast to the first hydrostatic stage. Still, the carbonated zone grew, and the porous zone slightly shrank, which suggests that  $\text{CC}$  precipitated preferentially inside the cement matrix rather than in the channel. To understand why  $\text{CC}$  precipitated in the channel during the first, but not the second hydrostatic phase, we consider the changes that the cement system underwent during the flow phase: (1) The carbonation front shifted  $\sim 0.4$  mm further into the bulk, so the source of calcium was farther away from the channel; (2) the porous silica zone grew larger, and thus the volume in which oversaturation is needed to induce precipitation has significantly increased (i.e., volume of the channel plus the volume of pore spaces); (3)  $\text{CC}$  precipitate was present in the channel. These changes increase the induction time required to achieve oversaturation of calcium and hydroxide ions, implying that  $\text{CC}$  could have started to precipitate if the second hydrostatic stage had lasted longer. The preferential precipitation inside the cement matrix suggests that, within the duration of the second hydrostatic phase, oversaturation was reached in the cement matrix only. When the flow rate was increased to 1 mL/h, the remaining  $\text{CC}$  in the channel started to dissolve. The dissolution rate during the second flow phase was almost identical to that in the first phase. The dissolution rate depends on the pH and saturation index in the channel, which is similar in both convective phases (Figure 3). The final increase in flow rate from 1 to 20 mL/h consistently produced an even faster dissolution of the remaining  $\text{CC}$  precipitate. A schematic overview of the chemical processes in the sample during the different stages of the  $\text{CO}_2$  exposure is depicted in Figure 5, highlighting that the  $\text{CC}$  precipitation or dissolution in the channel when exposed to carbonated water depends on the flow history: in the first period of flow, precipitation was observed and in the second period of flow, no precipitation was observed.

**Precipitation of  $\text{CaCO}_3$  in the Fracture.** A 3D visualization of the irregular “natural” fracture extending vertically throughout the cement sample at  $t = 0$  and  $t = 1200$  min is displayed in Figure 4, and a series of  $\mu$ -CT cross-sections of the fracture at different stages are shown in Figure 1 and S11. The natural fracture was almost fully closed from the beginning of the experiment, presumably due to the applied confinement stress, leaving only a few small cavities open. Although the fracture extended through the whole cement sample, only regions of the fracture near the top of the sample were filled by  $\text{CC}$  deposits (Figure S16).  $\text{CC}$  precipitation at the upper surface of the fracture, i.e., “self-sealing”, likely prevented the liquid flow from carbonating the fracture deeper inside the cement.

However,  $\text{CC}$  precipitation occurred in the individual fracture cavities when the diffusing  $\text{CO}_2$  front emanating

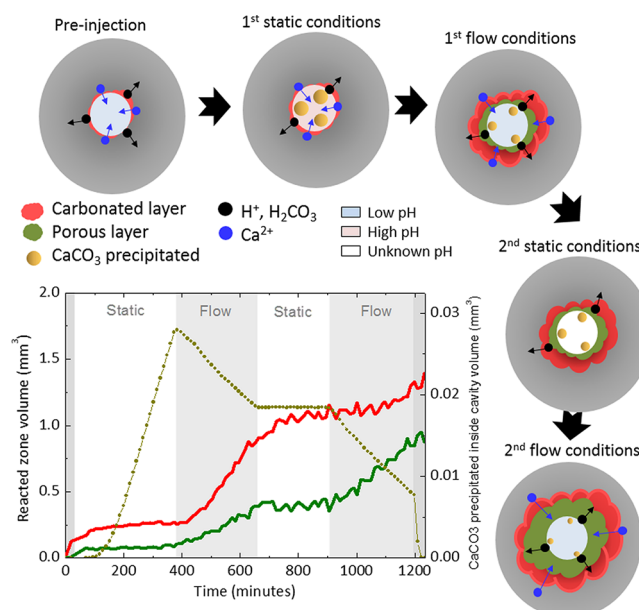


**Figure 5.** Schematic overview of the carbonation and self-sealing process of the sample during different stages of the  $\text{CO}_2$  exposure.

from the nearby channel reached them, cf. Figure 1c. Detailed analysis of the volume reduction due to the carbonation process for a chosen single cavity is depicted in Figure 4c. This specific cavity had a length and height of  $\sim 300$   $\mu\text{m}$  and a width of  $\sim 100$   $\mu\text{m}$ . Time-resolved volume filling of the very same cavity as depicted in Figure 1c is shown in Figure 4d. During the experiment, the cavity volume decreased by about 80%, mainly due to the precipitation of  $\text{CC}$ . The  $\mu$ -CT image analysis shows that the precipitation in this selected cavity took place after  $\sim 500$  min. (Figure S13). The time anticipated for self-sealing of a given cavity will depend on its position with respect to the  $\text{CO}_2$  exposed surfaces.

While the  $\text{CC}$  crystals precipitated in the channel were isolated and localized, the precipitates in the fracture formed a continuous lining along the surfaces of the fracture. The  $\text{CC}$  layer was deposited not only at the side where the progressing carbonation front first reached the fracture but evenly on all the fracture surfaces, filling almost the entire original volume of the fracture with  $\text{CC}$  (Figure S11). The difference in appearance of the  $\text{CC}$  precipitate in the fracture (continuous layer) and in the channel (discrete particles) may arise from  $\text{Ca}^{2+}$  concentration, degree of saturation, pH, and surface roughness. Intuitively, the concentration of  $\text{Ca}^{2+}$  in the isolated fracture will be higher compared to the channel through which fluid flow was forced. Typically, for high degrees of oversaturation,  $\text{CC}$  nucleation may proceed so fast that most dissolved material is used to constitute the nuclei, whereas little is available for crystal growth. On the contrary, for low values of oversaturation, nucleation may proceed slowly as most dissolved material is consumed by crystal growth.<sup>52</sup> Because of the small size and isolated conditions of the fracture, the pH inside the fracture is expected to be higher than in the channel; therefore, oversaturation may be reached at lower calcium concentrations. Indeed, it has been reported that at pH  $\sim 12$ , smaller crystals form compared to those at pH 9.<sup>53,54</sup> It is likely that the polymorphic form of the  $\text{CC}$  precipitate will also be affected by the different conditions in the fracture and the cavity, which in turn may contribute to a different morphology of the precipitate. The differences in surface morphology

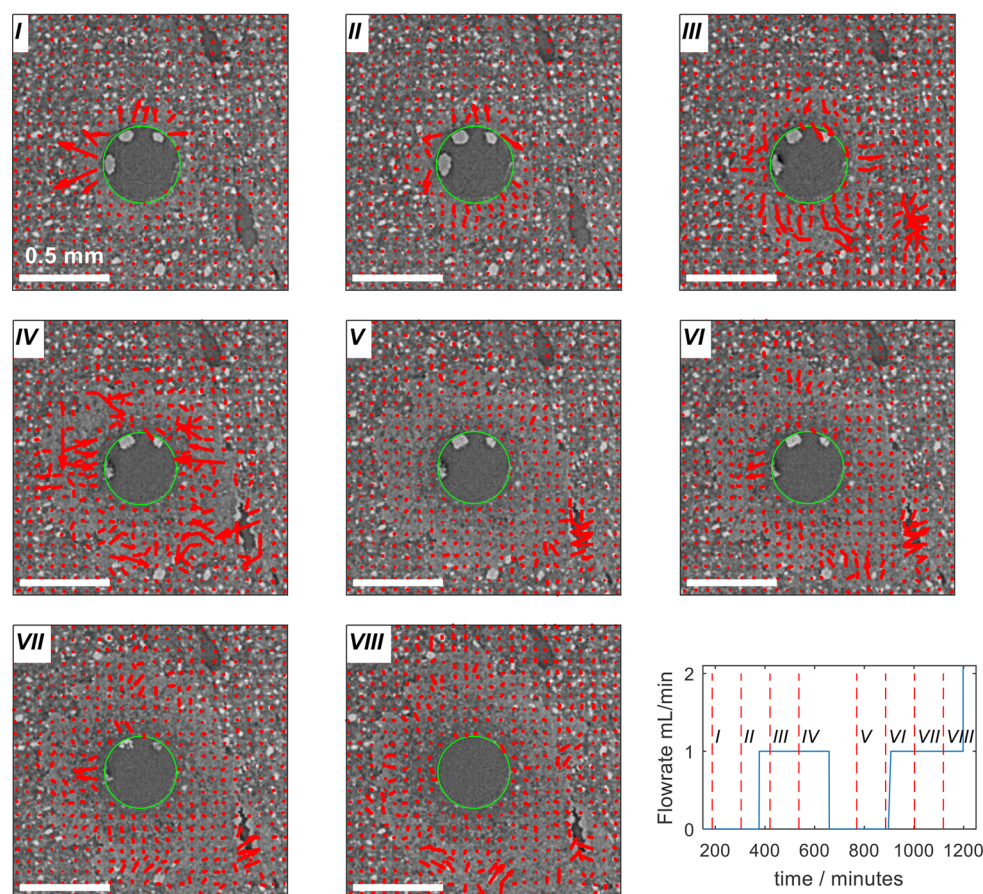


**Figure 6.** Time-resolved lateral distortions of the cement sample followed by DVC, near  $z = 2$  mm. The displacement fields show the difference between  $\mu$ -CT scans at the end and beginning of each interval, as indicated with Roman numerals. Note that essentially no changes are seen far from the channel, which is highlighted by a green circle. Stages I, II: Lateral expansion is observed from the start of the experiment near the artificial channel. Stage III: The carbonation front has reached the natural fracture in the down-right corner, which for the remainder of the experiment is seen to be monotonically squeezed. Stage IV exhibits high activity protruding further into the cement bulk, consistent with the liquid flow, while stage V (no-flow) only has small changes around the fracture. In stages VI–VII, the most notable observation is how the reaction has moved farther into the cement, leaving the surroundings of the channel effectively static. The magnitude of the displacement vectors is given in units of voxels multiplied by a factor 100, emphasizing that the distortions observed are indeed small.

between the smooth channel and the rough fracture might also have contributed to the qualitative differences in  $\text{CC}$  precipitate appearance. For rough surfaces, it is proposed that protrusions act as nucleation sites.<sup>55</sup> In addition, a roughness of  $\sim 20$   $\mu\text{m}$  is reported to increase the surface wettability, which is a parameter directly related with the rate of nucleation.<sup>56</sup> The difference of the solute concentration in the aqueous bulk and the concentration close to the crystal surface is higher in the channel, and that promotes the creation of bigger crystals.<sup>52</sup> As mentioned, the  $\text{CC}$  precipitate appeared as a smooth lining of the whole fracture surfaces and not only on the carbonated side where the carbonation front first reached the fracture. In fact, the growth rate of the  $\text{CC}$  layer was the same at the side facing the carbonation front as that at the side facing the nonreacted cement, suggesting that the oversaturation was relatively uniform across the fracture region.

**Geomechanical Analysis.** Digital volume correlation (DVC) was used to search for structural responses to the chemical reactions taking place within the sample. The 3D displacement field of the whole sample is fully consistent with the external triaxial stress state, revealing an expected axial compression, cf. SI. Subsequently, we focused on a comparably

small region near the channel within the sample, followed during eight distinct time intervals; see Figure 6. The fact that the specimen tilted slightly during the experiment necessitated the subtraction of the mean lateral displacement (effectively a sample translation at the small lengths scales of the investigated DVC volume) to reveal the finer details of the displacement field. Note that near the borders of the chosen DVC volume, i.e., far from the channel, essentially no changes are seen in any of the time intervals.

The DVC analysis indicates that local morphological changes were observed from the beginning of the experiment in the immediate surroundings of the channel, progressively protruding radially outward together with the carbonation front during the experiment (Figure 6). The deformation pattern surrounding the channel is understood to be induced by the local chemical alterations. During the time intervals of stagnant flow (particularly stage V), there is hardly any change to be seen around the channel.

The DVC analysis of the natural fractures observed in Figure 6 (lower right corner) supports the preceding discussion, highlighting that once the reaction front has reached the fracture, the fracture starts closing. Note that in the same figure (upper right corner), there is also another cavity of the natural



fracture, which is never reached by the carbonation front and consistently stays stationary throughout the experiment.

The observed changes seen by DVC may be explained by several possible mechanisms which require further investigations. The DVC technique calculates the incremental displacement components in the sample as macroscopic deformation progresses.<sup>40</sup> However, local modifications of the X-ray absorption properties due to chemical reaction may introduce a bias on the calculation of the incremental strain in the sample. Consequently, DVC allows the detection of locations with significant strain and/or chemical reaction, but a quantitative separation between these two components cannot readily be achieved. Because the bulk regions of the specimen are not reached by the carbonation front, we expect the DVC results in the bulk regions (see Figure S17) to stem from genuine mechanical deformations. Conversely, the region shown in Figure 6 is close to the channel, and the DVC changes are strongly correlated with the carbonation front, suggesting that a significant part of the signal picked up by the DVC analysis is caused by chemical reactions rather than mechanical displacement.

To the extent mechanical distortion is present, at least two mechanisms can be envisioned. First, the decrease of porosity in the carbonated zone<sup>57,58</sup> may induce a local increase of the elastic modulus due to phase transformation.<sup>50</sup> The cement becomes stronger macroscopically with carbonation while a reorganization of the microstructure takes place at small scale.<sup>59</sup> Second, by the force of crystallization,<sup>60</sup> a reorganization of the microstructure can be triggered by the stress caused by volume expansion of the carbonated cement, since carbonation of portlandite results in a net increase of volume.<sup>60</sup> Independent of the exact mechanism, intensity correlation-based DVC is evidently a powerful tool for quantitatively exploring minor structural changes inside the specimen.

**Environmental Implications.** Our study presents unprecedented time-lapse 3D imaging of the progressive degradation of Portland cement and the concomitant precipitation and dissolution of  $\text{CaCO}_3$  in leakage pathways with exposure to  $\text{sc-CO}_2$ . Importantly, the data was obtained in situ, showing the response to carbonated water at controlled flow rates under realistic reservoir conditions of high pressure and temperature. The alternated application of stagnant and flow-through conditions during the experiment aided delineation of precipitation versus dissolution-dominated regimes: information that can only be achieved through in situ laboratory experiments and potentially can be used for solving imminent environmental challenges related to  $\text{CO}_2$  storage. The methodology of increasingly realistic in situ imaging experiments combined with advanced modeling is destined to find many applications in the environmental and material sciences in the coming years. In the present study, experiments and geochemical modeling confirm that conditions with small  $\text{CO}_2$  flow rates promote the formation of the carbonated zone and subsequently precipitation of  $\text{CaCO}_3$  in large cavities. Conversely, in a leakage path with a comparably high  $\text{CO}_2$  flow rate, the formation of a weak and porous silica layer can severely degrade the cement. An important new finding relying on the in situ approach is the demonstration that the  $\text{CO}_2$  leakage risk from a well bore is severely impacted not only by the flow conditions but also by the flow history.

## ■ ASSOCIATED CONTENT

### Supporting Information

The Supporting Information is available free of charge at <https://pubs.acs.org/doi/10.1021/acs.est.0c00578>.

Information regarding sample preparation, experimental details, X-ray attenuation of cement phases, image processing, portlandite depleted zone, chemical numerical model,  $\mu$ -CT cross-section images of cement without color segmentation, additional volume calculations of the reacted zones in the cement, and mechanical response in the cement (PDF)

Movie showing cross-section slice at the middle of the sample during the  $\text{CO}_2$  exposure (AVI)

Movie showing the 3D visualization of precipitated  $\text{CaCO}_3$  in the channel during the  $\text{CO}_2$  exposure (The reconstructed tomograms are available from the corresponding author upon request.) (AVI)

## ■ AUTHOR INFORMATION

### Corresponding Authors

**Elvia A. Chavez Panduro** — Department of Physics, Norwegian University of Science and Technology (NTNU), 7491 Trondheim, Norway; SINTEF Energy Research, 7465 Trondheim, Norway; [orcid.org/0000-0003-3732-356X](https://orcid.org/0000-0003-3732-356X); Email: [elviachavezp@gmail.com](mailto:elviachavezp@gmail.com)

**Dag W. Breiby** — PoreLab, Department of Physics, Norwegian University of Science and Technology (NTNU), 7491 Trondheim, Norway; Department of Microsystems, University of South-Eastern Norway, 3184 Borre, Norway; Email: [dag.breiby@ntnu.no](mailto:dag.breiby@ntnu.no)

### Authors

**Benoît Cordonnier** — The Njord Centre, Department of Geosciences, University of Oslo, Oslo 0315, Norway; ESRF, European Synchrotron Radiation Facility, 38000 Grenoble, France

**Kamila Gawel** — SINTEF Industry, 7031 Trondheim, Norway

**Ingrid Børve** — Department of Physics, Norwegian University of Science and Technology (NTNU), 7491 Trondheim, Norway

**Jaisree Iyer** — Atmospheric Earth and Energy Division, Lawrence Livermore National Laboratory, Livermore, California 94550, United States; [orcid.org/0000-0002-1154-3030](https://orcid.org/0000-0002-1154-3030)

**Susan A. Carroll** — Atmospheric Earth and Energy Division, Lawrence Livermore National Laboratory, Livermore, California 94550, United States; [orcid.org/0000-0002-6456-3318](https://orcid.org/0000-0002-6456-3318)

**Leander Michels** — Department of Physics, Norwegian University of Science and Technology (NTNU), 7491 Trondheim, Norway; [orcid.org/0000-0002-0023-681X](https://orcid.org/0000-0002-0023-681X)

**Melania Rogowska** — Department of Chemistry, University of Copenhagen, 2100 Copenhagen Ø, Denmark

**Jessica Ann McBeck** — The Njord Centre, Department of Geosciences, University of Oslo, Oslo 0315, Norway

**Henning Osholm Sørensen** — Department of Chemistry, University of Copenhagen, 2100 Copenhagen Ø, Denmark; Department of Physics, Technical University of Denmark, 2800 Kongens Lyngby, Denmark; [orcid.org/0000-0002-7004-547X](https://orcid.org/0000-0002-7004-547X)

**Stuart D. C. Walsh** — Resources Engineering, Monash University, Melbourne, VIC 3800, Australia

**François Renard** — The Njord Centre, Department of Geosciences, University of Oslo, Oslo 0315, Norway; University

Grenoble Alpes, University Savoie Mont Blanc, CNRS, IRD, IFTTAR, ISTerre, 38000 Grenoble, France; [orcid.org/0000-0002-5125-5930](https://orcid.org/0000-0002-5125-5930)

Alain Gibaud – LUNAM, IMMM, UMR 6283 CNRS, Le Mans Université, 72085 Le Mans Cedex 09, France

Malin Torsæter – SINTEF Industry, 7031 Trondheim, Norway

Complete contact information is available at:

<https://pubs.acs.org/10.1021/acs.est.0c00578>

## Author Contributions

The experiment was planned and coordinated by A.G., E.A.C.P., M.T. and D.W.B. The sample cell was designed by F.R. and B.C. and constructed by Sanchez Technologies. The experiment at the synchrotron was carried out by B.C., L.M., M.R., H.O.S., and A.G., while the data analysis was done by E.A.C.P., I.B., K.G., and D.W.B. The geochemical modeling was done by J.I., S.D.C.W., and S.C. The mechanical analysis was performed by B.C., J.A.M., F.R., and D.W.B. E.A.C.P., K.G., and D.W.B. wrote the article. All authors have read and approved the final version of the manuscript.

## Notes

The authors declare no competing financial interest.

## ACKNOWLEDGMENTS

Elodie Boller at the European Synchrotron Radiation Facility (ESRF) in Grenoble, France, is thanked for technical support. This study received funding from the Norwegian Research Council (projects: CO<sub>2</sub>PLUG, grant 243765; Prometheus, grant 267775; and COMPMIC, 275182) and beam time was allocated at the ESRF. Data storage was provided by UNINETT Sigma2 - the National Infrastructure for High Performance Computing and Data Storage in Norway (project NS9073K). J.I. and S.C. from Lawrence Livermore National Laboratory performed the work under the Contract DE-AC52-07NA27344. H.O.S. received funding for travelling to the synchrotron facility from the Danish Agency for Science, Technology and Innovation via Danscatt. DWB thanks the Research Council of Norway for funding its Centres of Excellence funding scheme, project number 262644, Centre for Porous Media Laboratory.

## REFERENCES

- (1) IPCC, 2007: *Climate Change 2007: The Physical Science Basis*; p 996.
- (2) IPCC, 2005: *IPCC Special Report on Carbon Dioxide Capture and Storage*; p 442.
- (3) Viswanathan, H. S.; Pawar, R. J.; Stauffer, P. H.; Kaszuba, J. P.; Carey, J. W.; Olsen, S. C.; Keating, G. N.; Kavetski, D.; Guthrie, G. D. Development of a hybrid process and system model for the assessment of wellbore leakage at a geologic CO<sub>2</sub> sequestration site. *Environ. Sci. Technol.* **2008**, *42* (19), 7280–6.
- (4) Kutchko, B.; Strazisar, B. R.; Dzombak, D. A.; Lowry, G. V.; Thaulow, N. Degradation of Well Cement by CO<sub>2</sub> under Geologic Sequestration Conditions. *Environ. Sci. Technol.* **2007**, *41* (13), 13.
- (5) Mason, H. E.; Du Frane, W. L.; Walsh, S. D.; Dai, Z.; Charnvanichborikarn, S.; Carroll, S. A. Chemical and mechanical properties of wellbore cement altered by CO<sub>2</sub>-rich brine using a multianalytical approach. *Environ. Sci. Technol.* **2013**, *47* (3), 1745–52.
- (6) Huerta, N. J.; Hesse, M. A.; Bryant, S. L.; Strazisar, B. R.; Lopano, C. Reactive transport of CO<sub>2</sub>-saturated water in a cement fracture: Application to wellbore leakage during geologic CO<sub>2</sub> storage. *Int. J. Greenhouse Gas Control* **2016**, *44*, 276–289.

- (7) Kutchko, B. G.; Strazisar, B. R.; Huerta, N.; Lowry, G. V.; Dzombak, D. A.; Thaulow, N. CO<sub>2</sub> Reaction with Hydrated Class H Well Cement under Geologic Sequestration Conditions: Effects of Flyash Admixtures. *Environ. Sci. Technol.* **2009**, *43*, 3947–3952.
- (8) Rimmelé, G.; Barlet-Gouédard, V.; Porcherie, O.; Goffé, B.; Brunet, F. Heterogeneous porosity distribution in Portland cement exposed to CO<sub>2</sub>-rich fluids. *Cem. Concr. Res.* **2008**, *38* (8–9), 1038–1048.
- (9) Duguid, A.; Scherer, G. W. Degradation of oilwell cement due to exposure to carbonated brine. *Int. J. Greenhouse Gas Control* **2010**, *4* (3), 546–560.
- (10) Luquot, L.; Abdoulghafour, H.; Gouze, P. Hydro-dynamically controlled alteration of fractured Portland cements flowed by CO<sub>2</sub>-rich brine. *Int. J. Greenhouse Gas Control* **2013**, *16*, 167–179.
- (11) Mason, H. E.; Walsh, S. D.; DuFrane, W. L.; Carroll, S. A. Determination of diffusion profiles in altered wellbore cement using X-ray computed tomography methods. *Environ. Sci. Technol.* **2014**, *48* (12), 7094–100.
- (12) Cao, P.; Karpyn, Z. T.; Li, L. Self-healing of cement fractures under dynamic flow of CO<sub>2</sub>-rich brine. *Water Resour. Res.* **2015**, *51* (6), 4684–4701.
- (13) Carroll, S.; Carey, J. W.; Dzombak, D.; Huerta, N. J.; Li, L.; Richard, T.; Um, W.; Walsh, S. D. C.; Zhang, L. Review: Role of chemistry, mechanics, and transport on well integrity in CO<sub>2</sub> storage environments. *Int. J. Greenhouse Gas Control* **2016**, *49*, 149–160.
- (14) Kutchko, B. G.; Strazisar, B. R.; Lowry, G. V.; Dzombak, D. A.; Thaulow, N. Rate of CO<sub>2</sub> attack on hydrated Class H well cement under geologic sequestration conditions. *Environ. Sci. Technol.* **2008**, *42* (16), 6237–42.
- (15) Brunet, J.-P. L.; Li, L.; Karpyn, Z. T.; Kutchko, B. G.; Strazisar, B.; Bromhal, G. Dynamic Evolution of Cement Composition and Transport Properties under Conditions Relevant to Geological Carbon Sequestration. *Energy Fuels* **2013**, *27* (8), 4208–4220.
- (16) Walsh, S. D. C.; DuFrane, W. L.; Mason, H. E.; Carroll, S. A. Permeability of Wellbore-Cement Fractures Following Degradation by Carbonated Brine. *Rock Mechanics and Rock Engineering* **2013**, *46* (3), 455–464.
- (17) Liteanu, E.; Spiers, C. J. Fracture healing and transport properties of wellbore cement in the presence of supercritical CO<sub>2</sub>. *Chem. Geol.* **2011**, *281* (3–4), 195–210.
- (18) Matteo, E. N.; Huet, B.; Jové-Colón, C. F.; Scherer, G. W. Experimental and modeling study of calcium carbonate precipitation and its effects on the degradation of oil well cement during carbonated brine exposure. *Cem. Concr. Res.* **2018**, *113*, 1–12.
- (19) Iyer, J.; Walsh, S. D. C.; Hao, Y.; Carroll, S. A. Incorporating reaction-rate dependence in reaction-front models of wellbore-cement/carbonated-brine systems. *Int. J. Greenhouse Gas Control* **2017**, *59*, 160–171.
- (20) Cao, P.; Karpyn, Z. T.; Li, L. Dynamic alterations in wellbore cement integrity due to geochemical reactions in CO<sub>2</sub>-rich environments. *Water Resour. Res.* **2013**, *49* (7), 4465–4475.
- (21) Wigand, M.; Kaszuba, J. P.; Carey, J. W.; Hollis, W. K. Geochemical effects of CO<sub>2</sub> sequestration on fractured wellbore cement at the cement/caprock interface. *Chem. Geol.* **2009**, *265* (1–2), 122–133.
- (22) Guthrie, G. D.; Pawar, R. J.; Carey, J. W.; Karra, S.; Harp, D. R.; Viswanathan, H. S. The mechanisms, dynamics, and implications of self-sealing and CO<sub>2</sub> resistance in wellbore cements. *Int. J. Greenhouse Gas Control* **2018**, *75*, 162–179.
- (23) Brunet, J.-P. L.; Li, L.; Karpyn, Z. T.; Huerta, N. J. Fracture opening or self-sealing: Critical residence time as a unifying parameter for cement–CO<sub>2</sub>–brine interactions. *Int. J. Greenhouse Gas Control* **2016**, *47*, 25–37.
- (24) Newell, D. L.; Carey, J. W. Experimental evaluation of wellbore integrity along the cement-rock boundary. *Environ. Sci. Technol.* **2013**, *47* (1), 276–82.
- (25) Um, W.; Jung, H.; Kabilan, S.; Suh, D.; Fernandez, C. *Geochemical and Geomechanical Effects on Wellbore Cement Fractures*:

Data Information for Wellbore Reduced Order Mode; Pacific Northwest National Laboratory Richland: WA, January, 2014.

(26) Wolterbeek, T. K. T.; Peach, C. J.; Raoof, A.; Spiers, C. J. Reactive transport of CO<sub>2</sub>-rich fluids in simulated wellbore interfaces: Flow-through experiments on the 1–6 m length scale. *Int. J. Greenhouse Gas Control* **2016**, *54*, 96–116.

(27) Wolterbeek, T. K. T.; Ruckert, F.; van Moorsel, S. G.; Cornelissen, E. K. Reactive transport and permeability evolution in wellbore defects exposed to periodic pulses of CO<sub>2</sub>-rich water. *Int. J. Greenhouse Gas Control* **2019**, *91*, 102835.

(28) Han, W. S.; Lu, M.; McPherson, B. J.; Keating, E. H.; Moore, J.; Park, E.; Watson, Z. T.; Jung, N. H. Characteristics of CO<sub>2</sub>-driven cold-water geyser, Crystal Geyser in Utah: experimental observation and mechanism analyses. *Geofluids* **2013**, *13* (3), 283–297.

(29) Jung, H. B.; Kabilan, S.; Carson, J. P.; Kuprat, A. P.; Um, W.; Martin, P.; Dahl, M.; Kafentzis, T.; Varga, T.; Stephens, S.; Arey, B.; Carroll, K. C.; Bonneville, A.; Fernandez, C. A. Wellbore cement fracture evolution at the cement–basalt caprock interface during geologic carbon sequestration. *Appl. Geochem.* **2014**, *47*, 1–16.

(30) Kampman, N.; Burnside, N. M.; Shipton, Z. K.; Chapman, H. J.; Nicholl, J. A.; Ellam, R. M.; Bickle, M. J. Pulses of carbon dioxide emissions from intracrustal faults following climatic warming. *Nat. Geosci.* **2012**, *5* (5), 352–358.

(31) Watson, T. L. *Surface Casing Vent Flow Repair—A Process*. In *Petroleum Society's 5th Canadian International Petroleum Conference (55th Annual Technical Meeting)*, Calgary, Alberta, Canada, 2004.

(32) Carey, J. W.; Wigand, M.; Chipera, S. J.; WoldeGabriel, G.; Pawar, R.; Lichtner, P. C.; Wehner, S. C.; Raines, M. A.; Guthrie, G. D. Analysis and performance of oil well cement with 30 years of CO<sub>2</sub> exposure from the SACROC Unit, West Texas, USA. *Int. J. Greenhouse Gas Control* **2007**, *1* (1), 75–85.

(33) Crow, W.; Carey, J. W.; Gasda, S.; Brian Williams, D.; Celia, M. Wellbore integrity analysis of a natural CO<sub>2</sub> producer. *Int. J. Greenhouse Gas Control* **2010**, *4* (2), 186–197.

(34) Chavez Panduro, E. A.; Torsæter, M.; Gawel, K.; Bjørge, R.; Gibaud, A.; Yang, Y.; Bruns, S.; Zheng, Y.; Sørensen, H. O.; Breiby, D. W. In-Situ X-ray Tomography Study of Cement Exposed to CO<sub>2</sub> Saturated Brine. *Environ. Sci. Technol.* **2017**, *51* (16), 9344–9351.

(35) Renard, F.; Cordonnier, B.; Dysthe, D. K.; Boller, E.; Tafforeau, P.; Rack, A. A deformation rig for synchrotron microtomography studies of geomaterials under conditions down to 10 km depth in the Earth. *J. Synchrotron Radiat.* **2016**, *23* (4), 1030.

(36) Standard 10 B-2. (API), American Petroleum Institute.

(37) Paganin, D.; Mayo, S. C.; Gureyev, T. E.; Miller, P. R.; Wilkins, S. W. Simultaneous phase and amplitude extraction from a single defocused image of a homogeneous object. *J. Microsc.* **2002**, *206* (1), 33–40.

(38) Mirone, A.; Brun, E.; Gouillart, E.; Tafforeau, P.; Kieffer, J. The PyHST2 hybrid distributed code for high speed tomographic reconstruction with iterative reconstruction and a priori knowledge capabilities. *Nucl. Instrum. Methods Phys. Res., Sect. B* **2014**, *324*, 41–48.

(39) Walsh, S. D. C.; Mason, H. E.; Du Frane, W. L.; Carroll, S. A. Experimental calibration of a numerical model describing the alteration of cement/caprock interfaces by carbonated brine. *Int. J. Greenhouse Gas Control* **2014**, *22*, 176–188.

(40) Tudisco, E.; Andò, E.; Cailletaud, R.; Hall, S. A. TomoWarp2: A local digital volume correlation code. *SoftwareX* **2017**, *6*, 267–270.

(41) McBeck, J. A.; Cordonnier, B.; Vinciguerra, S.; Renard, F. Volumetric and Shear Strain Localization in Mt. Etna Basalt. *Geophys. Res. Lett.* **2019**, *46* (5), 2425–2433.

(42) McBeck, J. A.; Kobchenko, M.; Hall, S. A.; Tudisco, E.; Cordonnier, B.; Meakin, P.; Renard, F. Investigating the Onset of Strain Localization Within Anisotropic Shale Using Digital Volume Correlation of Time-Resolved X-Ray Microtomography Images. *Journal of Geophysical Research Solid Earth* **2018**, *123* (9), 7509–7528.

(43) Study of High Pressure High Temperature Zones in the Gulf of Mexico; 2017.

(44) Duguid, A.; Radonjic, M.; Scherer, G. W. *Degradation of Well Cements Exposed to Carbonated Brine*. In *Fourth Annual Conference on Carbon Capture and Sequestration Doeinetl*, 2005.

(45) Abdoulghafour, H.; Luquot, L.; Gouze, P. Characterization of the mechanisms controlling the permeability changes of fractured cements flowed through by CO<sub>2</sub>-rich brine. *Environ. Sci. Technol.* **2013**, *47* (18), 10332–8.

(46) Panduro, E. A. C.; Torsæter, M.; Gawel, K.; Bjørge, R.; Gibaud, A.; Yang, Y.; Sørensen, H. O.; Frykmanf, P.; Kjøllef, C.; Breiby, D. W. Closing of micro-cavities in well cement upon exposure to CO<sub>2</sub> brine. In *13th International Conference on Greenhouse Gas Control Technologies, GHGT-13*, Lausanne, Switzerland, 2016.

(47) Chavez Panduro, E. A.; Torsæter, M.; Gawel, K.; Bjørge, R.; Gibaud, A.; Bonnin, A.; Schlepütz, C. M.; Breiby, D. W. Computed X-ray Tomography Study of Carbonate Precipitation in Large Portland Cement Pores. *Cryst. Growth Des.* **2019**, *19* (10), 5850–5857.

(48) Andreassen, J.-P. Formation mechanism and morphology in precipitation of vaterite—nano-aggregation or crystal growth? *J. Cryst. Growth* **2005**, *274* (1–2), 256–264.

(49) Beuvier, T.; Calvignac, B.; Delcroix, G. J.-R.; Tran, M. K.; Kodjikian, S.; Delorme, N.; Bardeau, J.-F.; Gibaud, A.; Boury, F. Synthesis of hollow vaterite CaCO<sub>3</sub> microspheres in supercritical carbon dioxide medium. *J. Mater. Chem.* **2011**, *21*, 9757–9761.

(50) Oral, Ç. M.; Ercan, B. Influence of pH on morphology, size and polymorph of room temperature synthesized calcium carbonate particles. *Powder Technol.* **2018**, *339*, 781–788.

(51) de Moel, P. J.; van der Helm, A. W. C.; van Rijn, M.; van Dijk, J. C.; van der Meer, W. G. J. Assessment of calculation methods for calcium carbonate saturation in drinking water for DIN 38404–10 compliance. *Drinking Water Eng. Sci.* **2013**, *6* (2), 115–124.

(52) Luigi, M. *Geological Sequestration of Carbon Dioxide: Thermodynamics, Kinetics, and Reaction Path Modeling*. 1st ed.; Elsevier: 2007.

(53) Yu, J.; Lei, M.; Cheng, B.; Zhao, X. Effects of PAA additive and temperature on morphology of calcium carbonate particles. *J. Solid State Chem.* **2004**, *177* (3), 681–689.

(54) Declet, A.; Reyes, E.; Suarez, M. Calcium Carbonate Precipitation: A Review of the Carbonate Crystallization Process and Applications in Bioinspired Composites. *Review on Advanced Materials Science* **2016**, *44*, 87–107.

(55) Bohnet, M. Influence of the transport properties of the crystal/heat transfer surface interfacial on fouling behavior. *Chem. Eng. Technol.* **2003**, *26* (10), 1055–1060.

(56) Keysar, S.; Semiat, R.; Hasson, D.; Yahalom, J. Effect of Surface Roughness on the Morphology of Calcite Crystallizing on Mild Steel. *J. Colloid Interface Sci.* **1994**, *162*, 311–319.

(57) Savija, B.; Luković, M. Carbonation of cement paste: Understanding, challenges, and opportunities. *Construction and Building Materials* **2016**, *117*, 285–301.

(58) Johannesson, B.; Utgenannt, P. Microstructural changes caused by carbonation of cement mortar. *Cem. Concr. Res.* **2001**, *31* (6), 925–931.

(59) Lecampion, B.; Vanzo, J.; Ulm, F.; Huet, B.; Gernay, C.; Khafallah, I. *Evolution of Portland cement mechanical properties exposed to CO<sub>2</sub> rich fluids: investigation at different scales*. In *Mechanics and Physics of Porous Solids (MPPS) – A tribute to Prof Olivier Coussy*, Paris, France, 2011.

(60) Wolterbeek, T. K. T. *Impact of chemical and mechanical processes on wellbore integrity in CO<sub>2</sub> storage systems*. Utrecht University, Utrecht, The Netherlands, 2016.